The precipitation variability of wet and dry season at the interannual and interdecadal scales over eastern China (1901–2016): The impacts of the Pacific Ocean

Tao Gao[1, 4, 5], Fuqiang Cao [2, 3*], Li Dan[3], Ming Li[2], Xiang Gong[5], and Junjie Zhan[6]

[1] College of Urban Construction, Heze University, Heze 274000, China

[2] School of geosciences, Shanxi Normal University, Linfen 041000, China

[3] CAS Key Laboratory of Regional Climate-Environment Research for Temperate East Asia, Institute of Atmospheric Physics, Chinese Academy of Sciences, Beijing, China

[4] State Key Laboratory of Numerical Modeling for Atmospheric Sciences and Geophysical Fluid Dynamics, Institute of Atmospheric Physics, Chinese Academy of Sciences, Beijing 100029, China

[5] School of Mathematics and Physics, Qingdao University of Science and Technology, Qingdao 266061, China

[6] Shunyi Meteorological Service, Beijing, 101300, China

*Corresponding author address: Dr. Fuqiang Cao, 1 Gongyuan Road, Linfen 041000, P. R. China.

Email: wq2006126@126.com

Abstract: The spatiotemporal variability of rainfall in dry (October- March) and wet (April-September) seasons over eastern China is examined based on gridded rainfall dataset from University of East Angela Climatic Research Unit during 1901–2016. Principal component analysis is employed to identify the dominant variability modes, wavelet coherence is utilized to investigate the spectral features of leading modes of precipitation and their coherences with the large-scale modes of climate variability, and Bayesian dynamical linear model is adopted to quantify the time-varying correlations between climate variability modes and rainfall in dry and wet seasons. Results show that first and second principal components (PCs) account for 34.2% (16.1%) and 13.4% (13.9%) of variance in dry (wet) season, and their variations are roughly coincident with phase shifts of the El Niño-Southern Oscillation (ENSO) in both seasons. The anomalous moisture fluxes responsible for the occurrences of precipitation events in eastern China exhibit an asymmetry between high and light rainfall years in dry (wet) season. ENSO has a 4- to 8-year signal of the statistically positive (negative) association with rainfall during dry (wet) season over eastern China. The statistically significant positive (negative) associations between Pacific Decadal Oscillation (PDO) and precipitation are found with 9- to 15-year (4- to 7-year) signal. The impacts of PDO on rainfall in eastern China exhibit multiple time scales as compared to ENSO episodes, while PDO triggers a stronger effect on precipitation in wet season than dry half year. The interannual and interdecadal variations in rainfall over eastern China are substantially modulated by drivers originated from Pacific Ocean. In wet season, ENSO exerts a gradually weakening effect on eastern China rainfall from 1901 to 2016, while the effects of PDO decrease before 1980s, and then shift into increases after 2000s. The finding provides a metric for accessing the capability of climate models and guidance of seasonal prediction.

Keywords: Precipitation over eastern China; Principal component analysis; Wavelet spectral analysis; Bayesian dynamical linear model

1. Introduction

As a densely populated area with lots of industrial and agricultural activities, eastern China is frequently affected by the catastrophic floods and droughts derived from variability of precipitation events (Liu et al., 2015; Gao and Xie, 2016; Huang et al., 2017; Yang et al., 2017; Luo and Lau, 2018; Ge et al., 2019). For example, intense rainfall in southern China resulted in disastrous floods over the lower reach of Yangtze River basin (YRB) in 1991, 1996, 1998 and 1999. Seriously deficient precipitation in northern China caused a severe drought of 226 days without stream discharge over the Yellow River basin (Qian and Zhou, 2014; Xu et al., 2015; Zhang and Zhou, 2015). It is therefore of great importance to investigate the rainfall variability in eastern China and its associated physical mechanisms.

Both the observed and simulated results demonstrated that the variations in rainfall over eastern China are more closely correlated with the Pacific sea surface temperature (SST) anomalies as compared to Atlantic SST pattern, which plays a supplementary role on eastern China rainfall variability (Wang and Zhou, 2005; Huang et al., 2017; Yang et al., 2017). At the interannual scale, heavy rainfall events often occur over southern China during El Niño episodes (e.g., Zhang et al., 1996; Wang et al., 2000; He et al., 2017; Gao et al., 2020). While the variations in precipitation events over eastern China are remarkably impacted by tropical Pacific SST and western Pacific subtropical high at the interdecadal scale (WPSH, Chang et al., 2000a; Zhu et al., 2011; Li et al., 2019). Moreover, SST anomalies over the tropical Indian Ocean and tropical eastern Pacific also account for the shifts of the

positive-negative-positive rainfall patterns in eastern China via their influences on WPSH (Chang et al., 2000b; Hu et al., 2018). Thus, a better understanding of interannual and interdecadal changes stemming from the variability of air-sea interaction over the Pacific Ocean is instrumental to the interpretation and seasonal prediction for the rainfall variability over eastern China.

The El Niño-Southern Oscillation (ENSO) is a strong air-sea coupled mode at the interannual scale over the tropics, it is also the important source of interannual variability of the global climate system (Webster et al., 1998). ENSO significantly impacts rainfall over eastern China by means of the atmospheric teleconnections (e.g., Wang et al., 2008; Jin et al., 2016; Liu et al., 2016; Sun et al., 2017; Gao et al., 2017). Wang et al. (2000) proposed that the key system of Pacific-East Asian teleconnection responsible for linkages between ENSO and precipitation anomalies in eastern China is an anomalous low-level anticyclone located over the western North Pacific (WNP), which is induced by local air-sea interactions and large-scale equatorial heating anomalies. Wu et al. (2003) further argued that the similar positive correlation between springtime rainfall over the mid-lower reaches of YRB and ENSO is linked to the evolution of ENSO-related seasonal rainfall anomalies over the East Asia. Moreover, the summertime rainfall over the YRB and to its south is expected to be strengthened (weakened) during El Niño (La Niña) years. Huang and Wu (1989) documented that the drought in northern and southern China as well as flood over central China are associated with the developing stage of warm ENSO episodes, and the reversed relationship occurs in decaying stage of the warm events. These patterns

of rainfall in eastern China can also be plausibly related to strong convective activities in the Philippines, with the effects from western Pacific warm pool through shifting the WPSH northward (Huang and Sun, 1992; Jin et al., 2016). The latest research suggested that the patterns of seasonal rainfall anomaly in eastern China are impacted by the different types of La Niña decay, these are attributed to the responses of large-scale circulation anomalies induced by different types of La Niña episodes (Chen et al., 2019).

At the interdecadal scale, northern China experienced dry and wet alternations, with above-normal rainfall around the 1950s and severe droughts around the 1970s and 1980s. While the YRB and southern China suffered apparent shifts of precipitation patterns in the 1970s and 1990s (Zhu et al., 2015). A growing body of studies indicated that these shifts of rainfall distribution over eastern China are caused by the shifts in Pacific decadal oscillation (PDO) phases. Yang and Lau (2004) reported a close relationship between the positive PDO and decreasing trends of summertime rainfall events over eastern China. Based on surface wetness indices, Ma (2007) further pointed out an anti-correlation between rainfall in northern China and PDO phases, suggesting more droughts during positive phase of PDO, and vice versa. The strengthened (weakened) precipitation over the Huang-Huai (Yangtze) River basin from 2000 to 2008 in comparison with those during 1979-1999 is triggered by the transition from warm to cold phase of the PDO around the 2000s, which is attributed to the weakened westerly winds and warming over the Lake Baikal induced by negative PDO phase after 2000s (Zhu et al., 2011). The possible modulation of the

PDO on the East Asian summer monsoon (EASM) and East Asian winter monsoon (EAWM), which are associated with summer and winter rainfall changes in eastern China, respectively, has also documented in previous studies (e.g., Yu, 2013; Chen et al., 2013). Zhou et al. (2013) pointed out an anti-correlation between the PDO and EASM since 1950s, and negative phases of the PDO correspond to a stronger EASM with more precipitation events over northern China. A much stronger EASM tends to appear after a weak EAWM in positive phases of the PDO than that in negative phases of the PDO (Chen et al., 2013). Existing studies also reported the similar relationship between positive phase of the PDO and dryness in northern China, and revealed that a warm phase of PDO in the 1976/1977 resulted in a weakened EASM associated with aridity in northern China in the 1980s and 1990s (Qian and Zhou, 2014; Zhu et al., 2015; Yang et al., 2017; Gao and Wang, 2017). Furthermore, the relationship between interdecadal variability of rainfall patterns over eastern China and phase transitions of PDO is also identified and verified by coupled climate model simulations (e.g., Li et al., 2010; Yu et al., 2015).

Most previous studies that assessed the impacts of ENSO and PDO on eastern China rainfall are limited to relatively short dataset records. Ouyang et al. (2014) and Yang et al. (2017) performed century-scale analyses of the linkage between rainfall pattern across China and ENSO and PDO, while their time-varying relationships are not sufficiently considered. The latest research documented that rainfall over northern China displays an unstable relationship with ENSO at the centennial scale (Wang et al., 2020), particularly, the predictability of seasonal rainfall over the East Asia largely

depends on the relationship between large-scale modes and regional precipitation (Chan and Zhou, 2005). Moreover, the variations in climatological seasonal rainfall are employed in aforementioned analyses, while the main rainy season in China, in particularly for eastern China, does not follow conventional seasonal boundaries, which smears out natural variability of precipitation seasonality based on climatological seasons, since the rainfall in eastern China is principally concentrated during April–September (Bao 1987; Domroes and Peng 1988; Zhai et al., 2005). Usage of boreal standard seasons may therefore unavoidably break the natural rainy distribution at the temporal scale, affecting the robustness of the analytical results. Zhai et al. (2005) have investigated trends of precipitation extremes during wet season (April–September) and dry season (October–March) in China, and suggested that utilization of six months as the dry (wet) half year facilitates to characterize the variations in extreme events. While up to now, the issue on whether the ENSO and PDO can contribute to the interannual and interdecadal rainfall variability in major rainy seasons over eastern China remains unclear. In this study, we utilize April–September as the wet half year (wet season) and October–March as the dry half year (dry season), respectively, to fill the gap of detecting robust signals of the time-varying effects of ENSO and PDO on the precipitation variability in eastern China based on long-term datasets. Data and methods are described in section 2. The results are provided in section 3. Section 4 presents the discussion and conclusions.

2. Data and Methods

2.1 Data

A dataset of daily accumulated rainfall amount at 756 meteorological stations during 1960-2015 across China is employed in this study. This dataset is developed at Climate Data Center of the National Meteorological Center of the China Meteorological Administration (http://cdc.cma.gov.cn/dataSetDetailed.do), including almost all the first and second class national climatological stations. The accurate quality control procedures are conducted to check the temporal inhomogeneity and missing values, and screen the related stations in the following analyses, meaning that the stations having too many missing rainfall values are dropped. For example, a year is considered as the missing year if there exists more than 10% missing days, and a station with less than 5% missing years is retained. After these procedures, 436 stations meet these criteria and are retained in the subsequent analyses. Another rainfall dataset is a global land monthly precipitation dataset from University of East Angela Climatic Research Unit (CRU), which has a high resolution of $0.5° \times 0.5°$ over land from 1901 to 2016. The CRU data covers a longer period compared to observed counterpart, more information about this dataset is referred to Harris et al. (2014). The observed rainfall datasets at 436 stations are used to access the robustness of reliability and representativeness of the CRU gridded data with much longer time series over eastern China, since the long-term gridded precipitation data during 1901-2016 are more suitable for examining multi-decadal variability.

The reanalysis datasets are utilized to detect the physical mechanisms responsible for the interannual and interdecadal variability of the eastern China rainfall. We select monthly global circulation variables from National Centers for Environmental

Prediction/National Center for Atmospheric Research (NCEP/NCAR) Reanalysis data (Kalnay et al., 1996). SST data are obtained from the Hadley Centre, Met Office (Rayner et al., 2003). ENSO index is obtained from the Climate Prediction Center of NOAA (http://origin.cpc.ncep.noaa.gov/products/analysis_monitoring/ensostuff/detrend.nino34.ascii.txt). The PDO index is extracted from the Earth System Research Laboratory of NOAA (http://www. esrl.noaa.gov/psd/data/correlation/pdo.data/).

2.2 Method

2.2.1 Principle component analysis

The gridded CRU precipitation dataset is subjected to the principle component analysis (PCA), which is a widely applied method to extract the dominant temporal and spatial modes of the variability based on mutually correlated dataset. The leading principal component (PC) explains the most of variance, with the second PC decreases thereafter. Moreover, the leading PCs can reduce dimension of the original dataset, because they capture the most of variance. The detailed description of the PCA refers to Hannachi et al. (2007). To identify the effects of climate variability modes on changes in rainfall over eastern China, the correlations between the leading PCs and climate variability modes are calculated to examine the telecommunications. The composited maps of the atmospheric variables are analyzed to detect the physical mechanisms responsible for the rainfall variability by utilizing the high and light 25th percentile values of the daily rainfall in wet and dry seasons, respectively.

2.2.2 Wavelet coherence

The wavelet coherence is a widely employed technique, based on how coherent the cross-wavelet transform is in time frequency space. It can preferably access the detailed relationships between two time series with different time periods and disparate frequency ranges (e.g., Grinsted et al., 2004; Coulibaly and Burn, 2005). Given two particular time series x_n and y_n, the wavelet coherence of them can be expressed as

$$W^{XY} = W^{X} W^{Y*} \quad (1)$$

where $*$ represents their complex conjunction. Correspondingly, the cross-wavelet power can be expressed as $\left|W^{XY}\right|$. And complex argument arg $\left(W^{xy}\right)$ is considered as local relative phases between the time series x_n and y_n, which are applicative in both frequency and time domains. The wavelet coherence of the time series can be defined according to Torrence and Webster (1999).

$$R_n^2(s) = \frac{\left|S(s^{-1} W_n^{XY}(s))\right|^2}{S(s^{-1}\left|W_n^{X}(s)\right|^2) \cdot S\left(s^{-1}\left|W_n^{Y}(s)\right|^2\right)} \quad (2)$$

where S is the smoothing operator, which is further written as,

$$S_{time}(W) = S_{\text{scale}}(S_{\text{time}}(W_n(s))) \quad (3)$$

where S_{scale} and S_{time} denote the smoothing along wavelet scale axis and time, respectively. It is natural to design the smoothing operator so that it has a similar footprint as the wavelet.

The related codes for the wavelet coherence used in the present study can be freely downloaded from http://www.pol.ac.uk/home/research/waveletcoherence/. The wavelet coherence is used to investigate the correlations between ENSO/PDO and

rainfall over eastern China.

2.2.3 Bayesian dynamic linear model

The increases in amplitude of the SST anomaly patterns over the Pacific Ocean in the context of global warming trigger non-stationarity changes in regional rainfall (Wang et al., 2013; Krishnaswamy et al., 2015; Rajagopalan and Zagona, 2016). The Bayesian dynamic linear model (BDLM) is utilized to examine the non-stationarity and epochal fluctuations between the climate variability modes and rainfall in eastern China. The description of BDLM model as follows,

$$\begin{cases} y_t = \alpha_t + x_t\beta_t + v_t, & v_t \sim N(0,V_t) \\ \alpha_t = \alpha_{t-1} + \omega_{\alpha,t}, & \omega_{\alpha,t} \sim N(0,W_{\alpha,t}) \\ \beta_t = \beta_{t-1} + \omega_{\beta,t}, & \omega_{\beta,t} \sim N(0,W_{\beta,t}) \end{cases} \quad (4)$$

where y_t is the leading PCs of rainfall over eastern China, x_t is the covariate (climate variability modes, i.e., ENSO and PDO), and a_t and β_t are the dynamic intercept and slope coefficients at time t. ω_t is the corresponding evaluation error and W_t is the corresponding scalar greater than zero.

Unlike traditional linear regression methods that cannot characterize the robust time-varying relationship, BDLM can model and understand the non-stationarity in the relationships between large-scale modes of climate variability and regional precipitation with time. This method has been used to model monsoonal precipitation variability in India and China, and shows better performance and more interesting insights than the traditional regression method (Krishnaswamy et al., 2015; Gao et al., 2017). For the BDLM, the regression coefficient varies with time compared to the traditional regression, in which the coefficient remains fixed.

3. Results

3.1 Comparison between observed and CRU rainfall datasets

The variations in monthly and annual rainfall over eastern China based on both the observed stations and CRU gridded points from 1960 to 2015 are illustrated in Fig. 1. The monthly mean precipitation is shown in dashed lines and the climatological average is depicted in solid red lines (Fig. 1a, b). Fig. 1 shows that the climatological variability of observed rainfall along with months is quite similar to CRU gridded dataset. The slight disagreement is that the annual mean rainfall is larger and smaller than 80 mm for CRU and observed datasets, respectively. The climatological rainfall is greater (lesser) than annual mean value from April to September (October to March), consistent with the periods of wet (dry) season (half year) selected in this study. These changes in rainfall confirm that it is reasonable to categorize wet and dry seasons over eastern China. We further compare the time series of mean rainfall between observation and CRU datasets during wet and dry seasons (Fig. 1c, d), which indicates a strong level of similarity between observed and CRU datasets. High spatial similarity of the observed and CRU datasets during dry (Fig. 2a, c) and wet (Fig. 2b, d) seasons suggests that the spatial patterns from these two datasets are also consistent. In addition, the spectral analysis is also performed using the mean rainfall series of the two datasets (not shown) and the similar results are also obtained. Those indicate that the rainfall variability for CRU dataset coincides with observations over eastern China. We use CRU dataset since it covers a much longer period and is therefore more suitable to investigate the interdecadal variability. We present the following

analyses in wet and dry seasons, respectively, to provide a concise result.

3.2 Dry season

The two leading PCs explain 34.22% and 13.44% of the total variance, they together capture around 50% variance. Fig. 3 depicts the time series of first PC that is flipped for convenient comparison, which is suggestive of a well correspond with the spatial mean rainfall. The first two eigenvectors, including spatial components and corresponding PCs, are shown in Fig. 4. The spatial pattern of the first eigenvector exhibits similar magnitudes and signs, indicating that the dominant pattern is coherent in eastern China, especially over southern China and coastal regions (Fig. 4a), this may be associated with the propagation of the EAWM into mainland China. The second eigenvector displays a southeast-southwest dipole over southern China, this feature is coincident with the location and movement of the EASM (Ding et al., 2009). The time series of PCs also show considerable temporal changes with time, which are discussed in the spectral analysis.

Fig. 5 shows the correlation maps of climate variables and PC1 and PC2. Note that the signs of the PCs are flipped to ensure that the correlations are directly inferred as rainfall variability over eastern China. The correlation between PC1 and SSTs displays strong positive coefficients over the equatorial tropical Pacific and North Pacific. While the negative connections are mainly found over the South China Sea (SCS) and central-east Pacific, where it is featured by a La Niña SST pattern (Fig. 5a). This indicates that when the eastern Pacific is colder as it is the case in La Niña episodes, the strengthened convections may occur over southern China and adjacent

areas, leading to strengthened rainfall events, and vice versa in El Niño episodes. The pattern of correlation with SLP is inconsistent with ones for SSTs, the significant positive correlations are principally seen over the South Pacific and some tropical regions immediate close to the Indian and Pacific oceans (Fig. 5b). Whereas, some significant positive coefficients are located over the East China Sea, this may enhance the southeastern wind anomalies that transport more water vapor fluxes into southern China, providing conducive environmental backgrounds of forming more rainfall events. Considering correlations with the geopotential heights at 500 hPa (Fig. 5c), the significant negative coefficients over the tropical central-east Pacific suggest a weakened EAWM. When the EAWM weakens, the strengthened cold and dry air intrudes into southern China and converges with warm and wet air from the oceans, facilitating the occurrence of convective activities resulting in heavy precipitation events (Huang et al., 2018).

Correlation of SSTs with PC2 is reminiscent of the El Niño pattern, even though it is not evident (Fig. 5d), an indication suggests that El Niño episode yields a dipole pattern of the rainfall over southern China during dry season. The correlations with SLP exhibiting positive coefficients are mainly distributed in the North Pacific and Siberia, while the negative coefficients are principally situated over the equatorial Pacific and Indian Oceans (Fig. 5e). Correlation coefficient between PC2 and 500 hPa is relatively smaller and barely remarkable (Fig. 5f). Those imply that larger portion of the variability induced by climate variables occurs in the first mode.

Composited analyses of anomalous water vapor fluxes and divergence based on

313 highest 75th and lightest 25th percentile rainfall values, respectively, during dry
314 season are shown in Fig. 6. Considering the 25th percentile conditions, an anomalous
315 anticyclone appears over the WNP, while one branch of anomalous moisture fluxes to
316 the southern flank is transported eastward to eastern Pacific, meanwhile, another
317 branch is transported westward to Indian Ocean (Fig. 6a). As a result, the divergence
318 occurs over eastern China, which is not suitable for the formation of precipitation
319 events. The adverse phenomena are found for the 75th percentile events (Fig. 6b). The
320 westward transportation of anomalous water vapor fluxes is prominent over the
321 equatorial pacific, converging with the eastward transportation of moisture flux
322 anomalies from Indian Ocean over the SCS. Then the converged moisture fluxes are
323 transported northward, forming an anomalous cyclone over the WNP. The anomalous
324 water vapor fluxes over northern and western flanks of the WNP are transported into
325 eastern China, and anomalous terrestrial water vapor fluxes from Eurasia are also
326 transported into study domain. Those patterns provide favorable environmental
327 background and sufficient moisture supply for the formation of the convergence,
328 which is conducive to the occurrences of heavy rainfall events.

329 The wavelet coherence is performed on the PCs with large-scale ocean-atmosphere
330 circulation patterns to investigate the temporal variability of leading modes of rainfall
331 (Fig. 7). The local and global spectrums of PC1 indicate spectral peaks in the 1- to
332 4-year band and 6- to 10-year band further, which seems to be active during recent
333 decades (Fig. 7a). For PC2, the 1- to 4-year band is active before the middle part of
334 the twentieth century, while the 5- to 7-year band is concentrated in recent decades

(Fig. 7b). ENSO index (Niño3.4) exhibits a significant peak of 2- to 7-year period and a relatively weaker peak of 8- to 16-year period (Fig. 7c). Fig. 7e displays that ENSO has a positive association with rainfall from 1900 to 1930, with a 4- to 8-year signal. There is also a positive relationship from 1980 to 2010, with an 1- to 6-year signal. These suggest that ENSO has a statistically positive impact on precipitation over eastern China in dry season. Wavelet filtering of the PC1 in the 4- to 8-year period with ENSO being coherent (Fig. 7c) is also made and illustrated in Fig. 3 as the solid line. PDO has a statistically positive connection with rainfall from 1940 to 1970, with a 7- to 8-year signal. While a negative association is seen from 1980 to 2000, with an 8- to 9-year signal (Fig. 7f). Particularly, the PDO is closely correlated with precipitation over eastern China.

3.3 Wet season

The total variance captured by first two PCs is about 30%, with PC1 and PC2 explaining 16.06% and 13.93%, respectively, during wet season. These are smaller than total variances explained by two leading PCs of rainfall during dry season. The spatial mean precipitation is also captured by first PC (Fig. 8), which is flipped for easily comparing with spatial pattern. The solid line indicates the decadal smoother of first PC, and will be discussed later. While the low frequency of temporal variability is seen in Fig. 8. The spatial components and corresponding PCs of first two eigenvectors are shown in Fig. 9. A north-south dipole pattern is found for the first eigenvector, with strong negative values located over southern China (Fig. 9a), which has a close correlation with the variability of spatial mean precipitation (Fig. 8). This

rainfall pattern is also associated with the location and propagation of the EASM (Jin et al., 2016). In wet season, the northward advance of the EASM circulations is followed by three major rainy seasons sequentially: from May to mid-June, early summer rainy season occurs in southern China. Then the mei-yu season presents over the Yangtze-Huai river basins. The late summer rainy season ultimately forms over northern China (Ding and Chan, 2005). Correspondingly, multiple synoptic and climatological systems contribute to the occurrence of these rainfall events (Gao et al., 2016; Luo et al., 2016). The second eigenvector exhibits the magnitudes of the coherent signs in eastern China, with the peaks over the mid-lower reaches of YRB (Fig. 9b). Moreover, the first two PCs display considerable temporal changes (Fig. 9c, d) that are described in the discussion of spectral analysis.

The correlation map of PC1 with SSTs shows the strong positive coefficients over the North Pacific and western tropical Pacific (Fig. 10a), while some statistically negative correlations are distributed over the WNP. The positive correlations with SLP exhibiting statistical significance are seen over the eastern Pacific, and the negative values are found over the WNP and oceans to the eastern Australia (Fig. 10b). This is roughly an opposite correlation pattern of SLP compared to dry season (Fig. 5b and 10b). For 500 hPa, the positive correlations are mainly located over the WNP, with positive values principally situated over the equatorial western Pacific, which are weaker in comparison with the correlations in dry season. The correlation between SSTs and PC2 exhibits evident spatial features (Fig. 10d). Statistically significant negative coefficients are principally discovered over the eastern Pacific, reminiscent

379 of the La Niña episode, this is suggestive of the La Niña telecommunication
380 mechanisms responsible for the rainfall over eastern China during wet season. Note
381 that statistically significant positive coefficients are mainly distributed over the
382 northern Indian Ocean, resembling the Indian Ocean basin mode. To response the
383 basin-wide warming of Indian Ocean, the strengthened convective heating in the
384 tropical Indian Ocean will drive the Kelvin-wave-like eastern anomalies to the east.
385 Then, the anticyclonic shear of the Kelvin-wave-like easterlies may drive the
386 boundary layer divergence over the WNP by Ekman pumping, and therefore
387 suppresses convection there. These suppressed convections simulate an anomalous
388 anticyclone to the west. Ultimately, the anomalous anticyclone in the tropical WNP
389 intensifies rainfall in eastern China (Li et al., 2017; Cao et al., 2020). The correlation
390 of PC2 with SLP is much weaker compared to that of PC1, with significant negative
391 coefficients located over the far WNP (Fig. 10e). There also exists a weaker
392 correlation with 500 hPa in comparison with PC1, and negative values mainly situate
393 over the WNP (Fig. 10f).

394 Composited maps of moisture fluxes and divergence in high and light precipitation
395 years during wet season are illustrated in Fig. 11. Unlike the anomalous changes in
396 dry season (Fig. 6), the anomalous westward transportation of water vapor fluxes is
397 found over the equatorial Pacific for the lightest 25th percentile precipitation events,
398 while the water vapor anomalies that are transported from Indian Ocean into eastern
399 China are not apparent (Fig. 11a). However, anomalous moisture fluxes are
400 transported northeastward passing eastern China, and therefore fail to from

401 convergence there, which is not conducive to the occurrences of rainfall events. Fig.
402 11a shows that eastern China is principally dominated by divergence during light
403 rainfall years. For the highest 75th percentile precipitation events, an anomalous
404 cyclone appears over the WNP, even though it is relatively weak. The water vapor
405 anomalies originated from WNP converge with those from Eurasia over eastern China
406 (Fig. 11b). Most of the eastern China is dominated by convergence, providing suitably
407 environmental backgrounds of the occurrences of heavy rainfall events. In addition,
408 the anticyclone and cyclone are seen over the Indian Ocean during light and high
409 rainfall years, respectively, which is generally consistent with the Indian Ocean
410 capacitor effects on the Indo–western Pacific climate in summer (Xie et al., 2009).
411 The local and global spectrum of PC1 suggests the spectral peaks in the 1- to 5-year
412 and 6- to 10-year bands, as well as 16- to 32-year band further, these periods are
413 likely more active during recent decades (Fig. 12a). On the other hand, the PC2 shows
414 2- to 5-year and 5- to 8-year bands, as well as 16- to 24-year band. The first period
415 seems to be active in recent decades, and second and third periods are active from
416 1920 to 1980 (Fig. 12b). The ENSO index exhibits remarkable peaks of the 3- to
417 7-year period, which is active after 1950s (Fig. 12c). ENSO events have a statistically
418 negative relationship with rainfall over eastern China in wet season, with a 4- to
419 8-year signal, while other signals are not evident enough, although they occur
420 intermittently during the entire twentieth century (Fig. 12e). These suggest that the
421 modulation of ENSO on wet season precipitation is mainly concentrated at the
422 interannual scale, consistent with those in dry season. This also coincides with the

interannual band of the wavelet filtering of the PC1 (Fig. 8). Fig. 12f shows that PDO events have statistically significant positive associations with wet season rainfall from 1920 to 1940, with a 9- to 15-year signal. The significant negative connection with rainfall exhibits a 4- to 7-year signal from 1930 to 1950. It can be seen from Fig. 7f and Fig. 12f that PDO events have a stronger influence on rainfall in wet season than that in dry season.

The changing connections between leading modes of precipitation and large-scale modes of climate variability with time are accessed by BDLM (Fig. 13). We display the results that have discernable changes along with time, and ignore the results without discernable variations. The intercept from BDLM of PC1 and ENSO exhibits a slight increase from 1920 to 1960, then turns into a decrease condition and experiences zero value around the 1980s (Fig. 13a), suggesting that ENSO triggers a negative (positive) impact before (after) the 1980s, and the influences of ENSO become strengthened during recent decades. The intercept of PC2 and ENSO shows negative values, and is gradually decreasing with time, which indicates that the impacts of ENSO on PC2 are weakening during the entire century (Fig. 13b). Considering the effects of PDO, the positive connection between PDO and PC1 exhibits a decrease until 1980s, then the impacts of PDO on rainfall over eastern China are strengthening in recent decades (Fig. 13c). However, almost the opposite phenomenon is found for the connection between PC2 and PDO (Fig. 13d). The negative intercept is getting close to zero with time before 1980s, implying that the impact of PDO on PC1 is decreasing during this period. Then the positive connection

of PC2 and PDO become strengthened after 2000s, suggesting that the effect of PDO on PC2 is enhanced after this period. These results are important applications on the predictability of the rainfall events over eastern China based on the ENSO and PDO (Gao et al., 2017), since the ENSO and PDO has impacted the predictability of early summer monsoon precipitation in south China with the changes in connections between climate variability modes and rainfall (Chan and Zhou, 2005).

4. Discussion and conclusions

Space-time variability of rainfall during dry and wet seasons over eastern China is examined by utilizing PCA, wavelet coherence and BDLM, based on the CRU gridded and observed rainfall datasets. In the overlapping period of 1960-2015, these two rainfall datasets are consistent in their temporal and spatial patterns during wet and dry seasons over eastern China. While the CRU gridded data have a much longer period (1901-2016) and is more suitable to examine the interdecadal variability of rainfall.

The PCs exhibit notably temporal changes at the interannual and interdecadal scales. In dry season, the first and second eigenvectors account for 34.2% and 13.4% of variance, they exhibit coherent and dipole patterns of rainfall over southeastern and southern China, respectively, which are generally coincident with the shifts of ENSO phases. Particularly, the strengthened rainfall over southeastern China is associated with the La Niña episodes, and the dipole pattern of precipitation in southern China occurs during El Niño years. Moreover, the variations in rainfall over eastern China during dry season are also affected by the intensity of EAWM and the patterns of SLP.

In wet season, first and second eigenvectors show dipole and coherence of rainfall patterns, respectively, which are approximately contrary to that in dry season. And the two leading PCs account for 16.1% and 13.9% of variance. The circulations responsible for the changes in rainfall over eastern China are also generally opposite to those during dry season.

Composited analyses illustrate the southeastward and southwestward transportations of moisture flux anomalies from southern portion of eastern China, and there is no convergence occurred over study region for 25th percentile rainfall events during dry season. In the years with highest (75th percentile) rainfall events, the anomalous moisture fluxes from equatorial Pacific and Indian Ocean are transported into eastern China through SCS, leading to the convergence with the anomalous water vapor fluxes from WNP and Eurasia over eastern China, providing sufficient moisture supply and environmental backgrounds for the occurrences of precipitation events. In wet season, the anomalous variations in moisture fluxes are different with that during dry season. For the lightest rainfall years, the water vapor anomalies that are transported from equatorial Pacific pass through eastern China, this northeastward transportation of water vapor anomalies fails to form a convergence in study region. Thus, most of the eastern China is consequently dominated by the divergence. However, the opposite phenomena are found for the 75th percentile events, the water vapor anomalies from WNP converge with the anomalous moisture fluxes from Eurasia, they are transported southwestward into eastern China, resulting in heavy precipitation events. It is worth noting that the anticyclone and cyclone in

489 Indian Ocean also play an important role to the occurrences of rainfall events over
490 eastern China in addition to the forcing factors originated from Pacific Ocean (Xie et
491 al., 2009; Li et al., 2017).

492 ENSO has a statistically positive (negative) association with rainfall during dry
493 (wet) season in eastern China, with a 4- to 8-year signal. The impacts of ENSO on
494 rainfall are principally concentrated at the interannual scale in both dry and wet
495 seasons. PDO has a statistically positive (negative) relationship with rainfall in both
496 seasons, exhibiting a 7- to 8-year (8- to 9-year) signal in dry season. And the
497 statistically significant positive (negative) associations between PDO and
498 precipitation over eastern China is seen with 9- to 15-year (4- to 7-year) signal. In
499 short, the effects of PDO on rainfall show multiple time scales compared to these of
500 ENSO. Moreover, the PDO triggers a stronger impact on precipitation over eastern
501 China in wet season than dry season. Previous studies have revealed that PDO has a
502 significant effect on the movement of rainbelt over eastern China during the rainy
503 seasons, which influence the spatial distribution of rainfall events (i.e., southern flood
504 and northern drought) (Li et al., 2010; Gao et al., 2017). Our findings further confirm
505 the occurrences of those phenomena in eastern China at the interdecadal scale.

506 The analyses using BDLM suggest that there exists no significant time-varying
507 relationship between large-scale modes of climate variability and rainfall over eastern
508 China in dry season. In wet season, the intercept of ENSO and PC2 gradually
509 decreases with time, suggesting that the influences of ENSO on PC2 are gradually
510 weakening in the entire century. The effect of PDO on PC1 is decreasing before 1980s,

511 then shifts into positive connection after 2000s. These advance the understanding of
512 the time-varying linkage between climate variability modes and regional rainfall in
513 China. In addition, using a century-scale rainfall dataset allows us to obtain an insight
514 into the long-term time-varying correlations with precipitation events over eastern
515 China. The insights of spatiotemporal variability of rainfall over eastern China at
516 different time scales, and quantifying temporal variability of the strengths between
517 climate variability modes (ENSO and PDO) and rainfall will be of great importance
518 for developing skillful precipitation forecasting model (Zhang et al., 2014). Moreover,
519 BDLM provides a flexible regression method to incorporate the predictors with
520 varying strengths, the model parameters are therefore estimated dynamically at each
521 time, enabling to capture the time-varying predictors. The results in this study can
522 also be adopted to develop seasonal precipitation forecasting models. Particularly, the
523 asymmetry of the rainfall over eastern China and ENSO teleconnections in dry and
524 wet seasons indicate the different underlying causes during El Niño and La Niña
525 episodes, which can potentially improve the forecasting skills, these phenomena are
526 also true for different phases of PDO episodes. The physical and human
527 infrastructures over eastern China have suffered from severe floods and droughts,
528 therefore, the skillful hydroclimate projections of space–time variability of rainfall
529 will facilitate policy makers to develop the effective mitigation strategies.
530
531

Author contributions.

Gao T and Cao F designed all the experiments. Gao T and Cao F conducted all the experiments and analyzed the results. All the authors contributed to the preparation of the English editing.

Competing interests.

The authors declare that they have no conflict of interest.

Acknowledgments

We are heartily grateful to our editor, Prof. Dominic Mazvimavi, for his generous encouragement and great kindness for providing us with an opportunity to improve the quality of this manuscript. We cordially thank two anonymous reviewers for their professional comments and suggestions that were greatly helpful for further improvement of the quality of this manuscript. This study is jointly supported by Natural Science Foundation and Sci-tech development project of Shandong Province (No. ZR2018MD014; J18KA210), Key research and development plan of Shandong province in 2019 (No. 2019GGX105021), Project funded by China Postdoctoral Science Foundation (No. 119100582H; 1191005830), and Project of National Natural Science Foundation of China (No. 41630532).

552

553 ## References

554 Bao, C. L. : Synoptic Meteorology in China. China Ocean Press, 209 pp, 1987.

555 Cao, F., Gao, T., Dan, L., Ma, Z., Chen, X., Zou, L., and Zhang, L.: Synoptic-scale atmospheric
556 circulation anomalies associated with summertime daily precipitation extremes in the middle–lower
557 reaches of the Yangtze River Basin, *Clim Dynam*, 53, 3109-3129,
558 https://doi.org/10.1007/s00382-019-04687-3, 2020.

559 Chan, J. C., and Zhou, W.: PDO, ENSO and the early summer monsoon rainfall over south China,
560 *Geophys Res Lett*, 32, L08810, https://doi.org/10.1029/2004GL022015, 2005.

561 Chang, C. P., Zhang, Y., and Li, T.: Interannual and interdecadal variations of the East Asian summer
562 monsoon and tropical Pacific SSTs. Part I: Roles of the subtropical ridge, *J Climate*, 13, 4310-4325,
563 https://doi.org/10.1175/1520-0442(2000)013<4326:IAIVOT>2.0.CO;2, 2000a.

564 Chang, C. P., Zhang, Y., and Li, T:, Interannual and interdecadal variations of the East Asian summer
565 monsoon and tropical Pacific SSTs. Part II: Meridional structure of the monsoon, *J Climate*, 13,
566 4326-4340, https://doi.org/10.1175/1520-0442(2000)013<4326:IAIVOT>2.0.CO;2, 2000b.

567 Chen, S., Zhu, Z., Ge, Z., Kang, Z., and He, J.: The diversity of La Niña decay and the corresponding
568 spring and summer precipitation anomalies over eastern China, *Int J Climatol*, 11,
569 https://doi.org/10.1002/joc.6100, 2019.

570 Chen, W., Feng, J., and Wu, R.: Roles of ENSO and PDO in the link of the East Asian winter monsoon
571 to the following summer monsoon, *J Climate*, 26, 622-635,
572 https://doi.org/10.1175/JCLI-D-12-00021.1, 2013.

573 Coulibaly, P., and Burn, D. H.: Spatial and temporal variability of Canadian seasonal streamflows, *J*

574 *Climate*, 18, 191-210, https://doi.org/10.1175/JCLI-3258.1, 2005.

575 Domroes, M., and G. Peng: The Climate of China. SpringVerlag, 361 pp, 1988.

576 Ding, Y. H., and Chan, J. C.: The East Asian summer monsoon: an overview, *Meteorol Atmos Phys*, 89,

577 117-142, https://doi.org/10.1007/s00703-005-0125-z, 2005.

578 Ding, Y., Sun, Y., Wang, Z., Zhu, Y., and Song, Y.: Inter‐decadal variation of the summer

579 precipitation in China and its association with decreasing Asian summer monsoon Part II: Possible

580 causes, *Int J Climatol*, 29, 1926-1944, https://doi.org/10.1002/joc.1615, 2009.

581 Gao, T., Wang, H. J., and Zhou, T.: Changes of extreme precipitation and nonlinear influence of

582 climate variables over monsoon region in China, *Atmos Res*, 197, 379-389,

583 http://dx.doi.org/10.1016/j.atmosres.2017.07.017, 2017.

584 Gao, T., Xie, L., and Liu, B.: Association of extreme precipitation over the Yangtze River Basin with

585 global air‐sea heat fluxes and moisture transport, *Int J Climatol*, 36, 3020-3038,

586 https://doi.org/10.1002/joc.4534, 2016.

587 Gao, T., and Xie, L.: Spatiotemporal changes in precipitation extremes over Yangtze River basin,

588 China, considering the rainfall shift in the late 1970s, *Global Planet Change*, 147, 106-124,

589 https://doi.org/10.1016/j.gloplacha.2016.10.016, 2016.

590 Gao, T., and Wang, H.: Trends in precipitation extremes over the Yellow River basin in North China:

591 Changing properties and causes, *Hydrol Process*, 31, 2412-2428, https://doi.org/10.1002/hyp.11192,

592 2017.

593 Gao, T., Zhang, Q., and Luo, M.: Intensifying effects of El Niño events on winter precipitation

594 extremes in southeastern China, *Clim Dynam*, 54, 631-648,

595 https://doi.org/10.1007/s00382-019-05022-6, 2020.

Ge, J., You, Q., and Zhang, Y.: Effect of Tibetan Plateau heating on summer extreme precipitation in eastern China, *Atmos Res*, 218, 364-371, https://doi.org/10.1016/j.atmosres.2018.12.018, 2019.

Grinsted, A., Moore, J. C., and Jevrejeva, S.: Application of the cross wavelet transform and wavelet coherence to geophysical time series, *Nonlinear Proc Geoph*, 11, 561-566, https://doi.org/10.5194/npg-11-561-2004, 2004.

Hannachi, A., Jolliffe, I. T., and Stephenson, D. B.: Empirical orthogonal functions and related techniques in atmospheric science: A review, *Int J Climatol*, 27, 1119-1152, https://doi.org/10.1002/joc.1499, 2007.

Harris, I., Jones, P. D., Osborn, T. J., and Lister, D. H.: Updated high‐resolution grids of monthly climatic observations – the CRU TS3. 10 Dataset, *Int J Climatol*, 34, 623-642, https://doi.org/10.1002/joc.3711, 2014.

He, C., Lin, A., Gu, D., Li, C., Zheng, B., and Zhou, T.: Interannual variability of Eastern China Summer Rainfall: the origins of the meridional triple and dipole modes, *Clim Dynam*, 48, 683-696, https://doi.org/10.1007/s00382-016-3103-x, 2017.

Hu, C., Chen, D., Huang, G., and Yang, S.: Dipole Types of Autumn Precipitation Variability Over the Subtropical East Asia‐Western Pacific Modulated by Shifting ENSO, *Geophys Res Lett*, 45, 9123-9130, https://doi.org/10.1029/2018GL078982, 2018.

Huang, D., Dai, A., Zhu, J., Zhang, Y., and Kuang, X.: Recent Winter Precipitation Changes over Eastern China in Different Warming Periods and the Associated East Asian Jets and Oceanic Conditions, *J Climate*, 30, 4443–4462, https://journals.ametsoc.org/doi/10.1175/JCLI-D-16-0517.1, 2017.

Huang, R., and Sun, F.: Impacts of the tropical western Pacific on the East Asian summer monsoon,

618 *Journal of the Meteorological Society of Japan. Ser. II*, 70, 243-256,
619 http://dx.doi.org/10.3878/j.issn.1006-9895.2006.06.01, 1992.
620 Huang, R., and Wu, Y.: The influence of ENSO on the summer climate change in China and its
621 mechanism, *Adv Atmos Sci*, 6, 21-32, https://doi.org/10.1007/BF02656915, 1989.
622 Huang, W., He, X., Yang, Z., Qiu, T., Wright, J. S., Wang, B., and Lin, D.: Moisture sources for
623 wintertime extreme precipitation events over South China during 1979–2013, *Journal of*
624 *Geophysical Research: Atmospheres*, 123, 6690-6712, https://doi.org/10.1029/2018JD028485, 2018.
625 Jin, D., Hameed, S. N., and Huo, L.: Recent changes in ENSO teleconnection over the western Pacific
626 impacts the eastern China precipitation dipole, *J Climate*, 29, 7587-7598,
627 https://doi.org/10.1175/JCLI-D-16-0235.1, 2016.
628 Kalnay, E., Kanamitsu, M., Kistler, R., Collins, W., Deaven, D., Gandin, L., Iredell, M., Saha, S.,
629 White, G., and Woollen, J.: The NCEP/NCAR 40-year reanalysis project, *B Am Meteorol Soc*, 77,
630 437-471, https://doi.org/10.1175/1520-0477(1996)077<0437:TNYRP>2.0.CO;2, 1996.
631 Krishnaswamy, J., Vaidyanathan, S., Rajagopalan, B., Bonell, M., Sankaran, M., Bhalla, R. S., and
632 Badiger, S.: Non-stationary and non-linear influence of ENSO and Indian Ocean Dipole on the
633 variability of Indian monsoon rainfall and extreme rain events, *Clim Dynam*, 45, 175-184,
634 *https://doi.org/10.1007/s00382-014-2288-0,* 2015.
635 Lei, Y. U.: Potential correlation between the decadal East Asian summer monsoon variability and the
636 Pacific decadal oscillation, *Atmospheric and Oceanic Science Letters*, 6, 394-397,
637 https://doi.org/10.3878/j.issn.1674-2834.13.0040, 2013.
638 Li, H., Dai, A., Zhou, T., and Lu, J.: Responses of East Asian summer monsoon to historical SST and
639 atmospheric forcing during 1950–2000, *Clim Dynam*, 34, 501-514,

https://doi.org/10.1007/s00382-008-0482-7, 2010.

Li, Y., Ma, B., Feng, J., and Lu, Y.: Influence of the strongest central Pacific El Niño – Southern Oscillation events on the precipitation in eastern China, *Int J Climatol*, 39, 3076-3090, https://doi.org/10.1002/joc.6004, 2019.

Li, T., Bin, W., Bo, W. U., Tianjun, Z., and Chih-Pei Chang, R. Z.: Theories on Formation of an Anomalous Anticyclone in Western North Pacific during El Niño: A Review, *Journal of Meteorological Research*, 31, 987-1006, https://doi.org/10.1007/s13351-017-7147-6, 2017.

Liu, J., Wang, H., Lu, E., and Kumar, A.: Decadal modulation of East China winter precipitation by ENSO, *Clim Dynam*, 1-15, https://doi.org/10.1007/s00382-016-3427-6, 2016.

Liu, R., Liu, S. C., Cicerone, R. J., Shiu, C., Li, J., Wang, J., and Zhang, Y.: Trends of extreme precipitation in eastern China and their possible causes, *Adv Atmos Sci*, 32, 1027-1037, https://doi.org/10.1007/s00376-015-5002-1, 2015.

Luo, M., and Lau, N. C.: Increasing heat stress in urban areas of eastern China: Acceleration by urbanization, *Geophys Res Lett*, 45, 13-60, https://doi.org/10.3390/su11123413, 2018.

Luo, Y., Wu, M., Ren, F., Li, J., and Wong, W.: Synoptic situations of extreme hourly precipitation over China, *J Climate*, 29, 8703-8719, https://doi.org/10.1175/JCLI-D-16-0057.1, 2016.

Ma, Z.: The interdecadal trend and shift of dry/wet over the central part of North China and their relationship to the Pacific Decadal Oscillation (PDO), *Chinese Sci Bull*, 52, 2130-2139, https://doi.org/10.1007/s11434-007-0284-z, 2017.

Ouyang, R., Liu, W., Fu, G., Liu, C., Hu, L., and Wang, H.: Linkages between ENSO/PDO signals and precipitation, streamflow in China during the last 100 years, *Hydrol Earth Syst Sc*, 18, 3651-3661, https://doi.org/10.5194/hess-18-3651-2014, 2014.

662 Qian, C., and Zhou, T.: Multidecadal variability of North China aridity and its relationship to PDO
663 during 1900 – 2010, *J Climate*, 27, 1210-1222, https://doi.org/10.1175/JCLI-D-13-00235.1, 2014.
664 Rajagopalan, B., and Zagona, E.: Space–time variability of Indonesian rainfall at inter-annual and
665 multi-decadal time scales, *Clim Dynam*, 47, 2975-2989,
666 http://dx.doi.org/10.1007/s00382-016-3008-8, 2016.
667 Rayner, N. A., Parker, D. E., Horton, E. B., Folland, C. K., Alexander, L. V., Rowell, D. P., Kent, E. C.,
668 and Kaplan, A.: Global analyses of sea surface temperature, sea ice, and night marine air temperature
669 since the late nineteenth century, *Journal of Geophysical Research: Atmospheres*, 108.4407,
670 https://doi.org/10.1029/2002JD002670, 2003.
671 Sun, Q., Miao, C., Qiao, Y., and Duan, Q.: The nonstationary impact of local temperature changes and
672 ENSO on extreme precipitation at the global scale, *Clim Dynam*, 49, 4281-4292,
673 https://doi.org/10.1007/s00382-017-3586-0, 2017.
674 Torrence, C., and Webster, P. J.: Interdecadal changes in the ENSO–monsoon system, J Climate, 12,
675 2679-2690, https://doi.org/10.1175/1520-0442(1999)012<2679:ICITEM>2.0.CO;2, 1999.
676 Wang, B., Liu, J., Kim, H., Webster, P. J., Yim, S., and Xiang, B.: Northern Hemisphere summer
677 monsoon intensified by mega-El Niño/southern oscillation and Atlantic multidecadal oscillation,
678 *Proceedings of the National Academy of Sciences*, 110, 5347-5352,
679 https://doi.org/10.1073/pnas.1219405110, 2013.
680 Wang, B., Wu, R., and Fu, X.: Pacific-East Asian teleconnection: how does ENSO affect East Asian
681 climate? *J Climate*, 13, 1517-1536,
682 https://doi.org/10.1175/1520-0442(2000)013<1517:PEATHD>2.0.CO;2, 2000.
683 Wang, B., Luo, X., and Liu, J.: How Robust is the Asian Precipitation–ENSO Relationship during the

684 Industrial Warming Period (1901–2017)? J Climate, 33, https://doi.org/10.1175/JCLI-D-19-0630.1,
685 2779-2792, 2020.
686 Wang, L., Chen, W., and Huang, R.: Interdecadal modulation of PDO on the impact of ENSO on the
687 East Asian winter monsoon, *Geophys Res Lett*, 35, doi: 10.1029/2008GL035287,
688 https://doi.org/10.1029/2008GL035287, 2008.
689 Wang, Y., and Zhou, L.: Observed trends in extreme precipitation events in China during 1961 – 2001
690 and the associated changes in large-scale circulation, *Geophys. Res. Lett*, 32, L9707,
691 https://doi.org/10.1029/2005GL022574, 2005.
692 Webster, P. J., Magana, V. O., Palmer, T. N., Shukla, J., Tomas, R. A., Yanai, M., and Yasunari, T.:
693 Monsoons: Processes, predictability, and the prospects for prediction, *Journal of Geophysical*
694 *Research: Oceans*, 103, 14451-14510, https://doi.org/10.1029/97JC02719, 1998.
695 Wu, R., Hu, Z., and Kirtman, B. P.: Evolution of ENSO-related rainfall anomalies in East Asia, *J*
696 *Climate*, 16, 3742-3758, https://doi.org/10.1175/1520-0442(2003)016<3742:EOERAI>2.0.CO;2,
697 2003.
698 Xie, S., Hu, K., Hafner, J., Tokinaga, H., Du, Y., Huang, G., and Sampe, T.: Indian Ocean capacitor
699 effect on Indo-western Pacific climate during the summer following El Niño, *J Climate*, 22, 730-747,
700 https://doi.org/10.1175/2008JCLI2544.1, 2009.
701 Xiao, M., Zhang, Q., and Singh, V. P.: Influences of ENSO, NAO, IOD and PDO on seasonal
702 precipitation regimes in the Yangtze River basin, China, *Int J Climatol*, 35, 3556-3567,
703 https://doi.org/10.1002/joc.4228, 2015.
704 Xu, K., Yang, D., Yang, H., Li, Z., Qin, Y., and Shen, Y.: Spatio-temporal variation of drought in
705 China during 1961 – 2012: A climatic perspective, *J Hydrol*, 526, 253-264,

https://doi.org/10.1016/j.jhydrol.2014.09.047, 2015.

Yang, F., and Lau, K. M.: Trend and variability of China precipitation in spring and summer: linkage to sea‐surface temperatures, *Int J Climatol*, 24, 1625-1644, https://doi.org/10.1002/joc.1094, 2004.

Yang, Q., Ma, Z., Fan, X., Yang, Z., Xu, Z., and Wu, P.: Decadal Modulation of Precipitation Patterns over Eastern China by Sea Surface Temperature Anomalies, *J Climate*, 30, 7017-7033, https://doi.org/10.1175/JCLI-D-16-0793.1, 2017.

Yang, Q., Ma, Z., and Xu, B.: Modulation of monthly precipitation patterns over East China by the Pacific Decadal Oscillation, *Climatic Change*, 144, 405-417, https://doi.org/10.1007/s10584-016-1662-9, 2017.

Yu, L., Furevik, T., Otterå, O. H., and Gao, Y.: Modulation of the Pacific Decadal Oscillation on the summer precipitation over East China: a comparison of observations to 600-years control run of Bergen Climate Model, *Clim Dynam*, 44, 475-494, https://doi.org/10.1007/s00382-014-2141-5, 2015.

Zhai, P., Zhang, X., Wan, H., and Pan, X.: Trends in total precipitation and frequency of daily precipitation extremes over China, *J Climate*, 18, 1096-1108, https://doi.org/10.1175/JCLI-3318.1, 2005.

Zhang, W., Jin, F. F., and Turner, A.: Increasing autumn drought over southern China associated with ENSO regime shift, *Geophys Res Lett*, 41, 4020-4026, https://doi.org/10.1002/2014GL060130, 2014.

Zhang, L., and Zhou, T.: Drought over East Asia: a review, *J Climate*, 28, 3375-3399, https://doi.org/10.1175/JCLI-D-14-00259.1, 2015.

Zhang, R., Sumi, A., and Kimoto, M.: Impact of El Niño on the east Asian monsoon: A Diagnostic Study of the '86/87 and '91/92 Events, *Journal of the Meteorological Society of Japan. Ser. II*, 74,

728 49-62, https://doi.org/10.2151/jmsj1965.74.1_49, 1996.

729 Zhu, Y., Wang, H., Ma, J., Wang, T., and Sun, J.: Contribution of the phase transition of Pacific
730 Decadal Oscillation to the late 1990s' shift in East China summer rainfall, *Journal of Geophysical*
731 *Research: Atmospheres*, 120, 8817-8827, https://doi.org/10.1002/2015JD023545, 2015.

732 Zhu, Y., Wang, H., Zhou, W., and Ma, J.: Recent changes in the summer precipitation pattern in East
733 China and the background circulation, Clim Dynam, 36, 1463-1473,
734 https://doi.org/10.1007/s00382-010-0852-9, 2011.

735 Zhou T, Song F, Lin R, Chen X, Chen X.: Explaining extreme events of 2012 from a climate
736 perspective. *Bull Am Meteorol Soc*, 94:S1–S74, https://doi.org/10.1175/BAMS-D-13-00085.1, 2013.

737

738

Figure captions

Figure 1. Annual climatological rainfall at all stations (STN) and grid (CRU) points shown as grey lines and their mean in a solid red line, (a) observation and (b) CRU. Seasonal mean precipitation anomalies from observation (black) and CRU (blue), (c) dry season and (d) wet season.

Figure 2. Spatial distribution of seasonal mean precipitation (mm/month) during 1960-2015 over eastern China from observation and CRU datasets, (a) and (c) are for dry season; (b) and (d) are for wet season.

Figure 3. Standardized time series of all dry season precipitation over eastern China as shown in red dashed line, the black dots denote flipped PC1 and the blue lines denote the decadal features of dry season precipitation.

Figure 4. (a) The first and (b) second EOFs for the rainfall in dry season. (c) The first and (d) second principal components (PCs) correspond to these EOFs from the rainfall in dry season. Both time series are normalized with respect to the corresponding standard deviations.

Figure 5. Correlation coefficients in dry season. (a) sea surface temperature and PC1, (b) mean sea level pressure with PC1, (c) geopotential height at the 500 hPa and PC1, (c) sea surface temperature and PC2, (e) mean sea level pressure with PC2 and (f) geopotential height at the 500 hPa with PC2. Hatching denotes the regions with statistical significance at the 95% confidence level. Black rectangle denotes the eastern China.

Figure 6. Vertically integrated water vapor anomalies (vector) and water vapor flux divergence (shading) composited from the lightest 25th (a) and highest 75th (b) percentile rainfall events in dry season. The water vapor flux unit is kg m^{-1} s^{-1} for and the water vapor flux divergence is kg m^{-2} s^{-1}. Green rectangle denotes the eastern China.

Figure 7. Wavelet spectra for dry season. (a) PC1, (b) PC2, (c) Niño3.4 index, (d) PDO index, (e) wavelet spectral coherence of PC1 and Niño3.4, and (f) wavelet spectral coherence of PC2 and PDO. The global spectra are shown on the right side of

768 the time varying wavelet spectra and, the black lines denote the statistical significance
769 at the 95% confidence level.
770 Figure 8. Standardized time series of all wet season precipitation over eastern China
771 as shown in red dashed line, the black dots denote flipped PC1 and the blue lines
772 denote the decadal features of wet season precipitation.
773 Figure 9. (a) The first and (b) second EOFs for the rainfall in wet season. (c) The first
774 and (d) second principal components (PCs) correspond to these EOFs from the
775 rainfall in wet season. Both time series are normalized with respect to the
776 corresponding standard deviations
777 Figure 10. Correlation coefficients in wet season. (a) sea surface temperature and PC1,
778 (b) mean sea level pressure with PC1, (c) geopotential height at the 500 hPa and PC1,
779 (c) sea surface temperature and PC2, (e) mean sea level pressure with PC2 and (f)
780 geopotential height at the 500 hPa with PC2. Hatching denotes the regions with
781 statistical significance at the 95% confidence level. Black rectangle denotes the
782 eastern China.
783 Figure 11. Vertically integrated water vapor anomalies (vector) and water vapor flux
784 divergence (shading) composited from the lightest 25th (a) and highest 75th (b)
785 percentile rainfall events in wet season. The water vapor flux unit is kg m^{-1} s^{-1} for and
786 the water vapor flux divergence is kg m^{-2} s^{-1}. Black rectangle denotes the eastern
787 China.
788 Figure 12. Wavelet spectra for wet season. (a) PC1, (b) PC2, (c) Niño3.4 index, (d)
789 PDO index, (e) wavelet spectral coherence of PC1 and Niño3.4, and (f) wavelet
790 spectral coherence of PC2 and PDO. The global spectra are shown on the right side of
791 the time varying wavelet spectra and, the black lines denote the statistical significance
792 at the 95% confidence level.
793 Figure 13. Changes in the relationships between rainfall and ENSO/PDO over time
794 during 1901-2015. Black solid lines denote the estimated time-varying slopes, along
795 with 25th and 75th percentile credible interval lines (red dotted lines) from the
796 Bayesian dynamic linear model analysis.
797

798

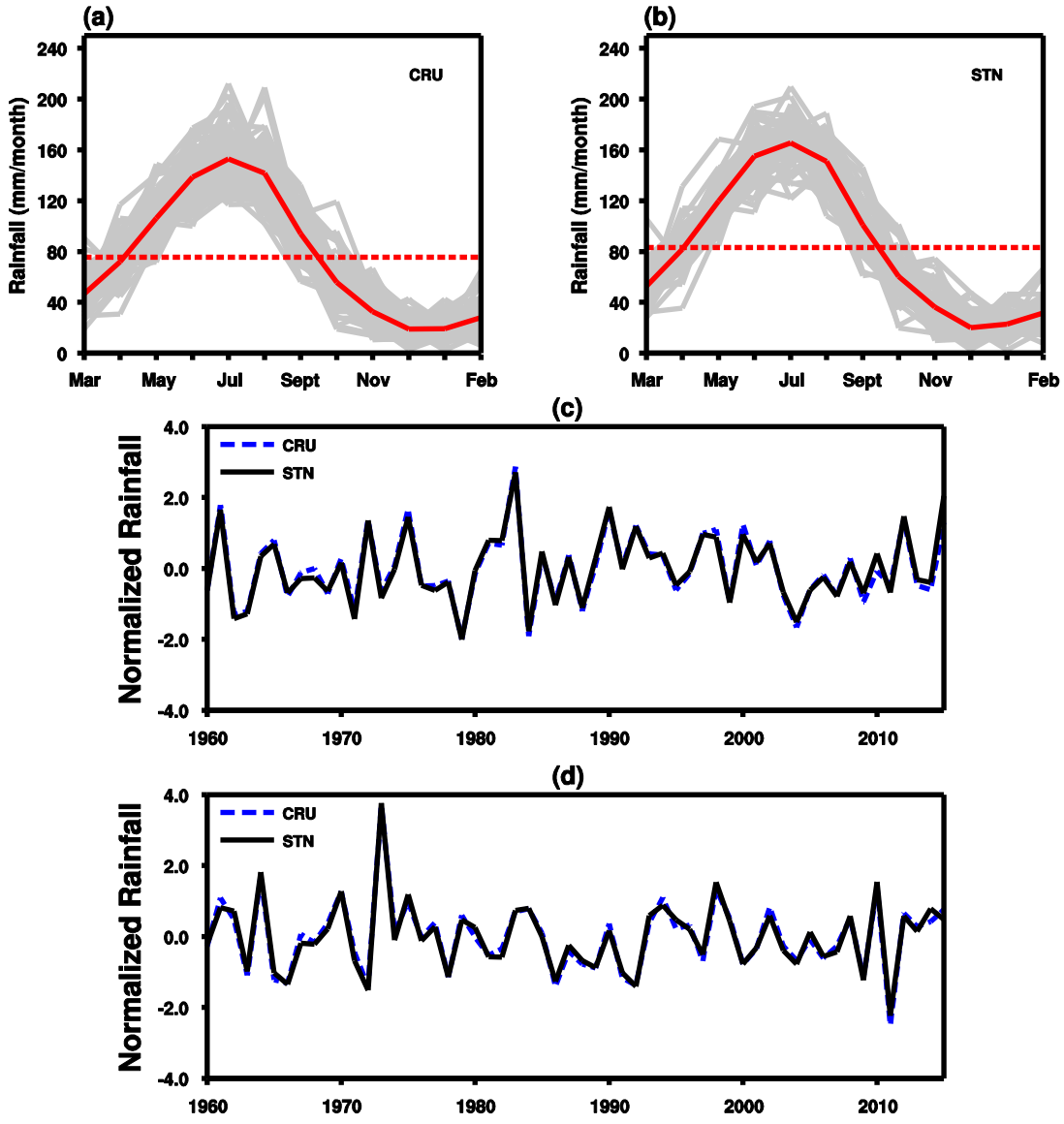

799

800 Figure 1. Annual climatological rainfall at all stations (STN) and grid (CRU) points
801 shown as grey lines and their mean in a solid red line, (a) observation and (b) CRU.
802 Seasonal mean precipitation anomalies from observation (black) and CRU (blue), (c)
803 dry season and (d) wet season.

804

805

806

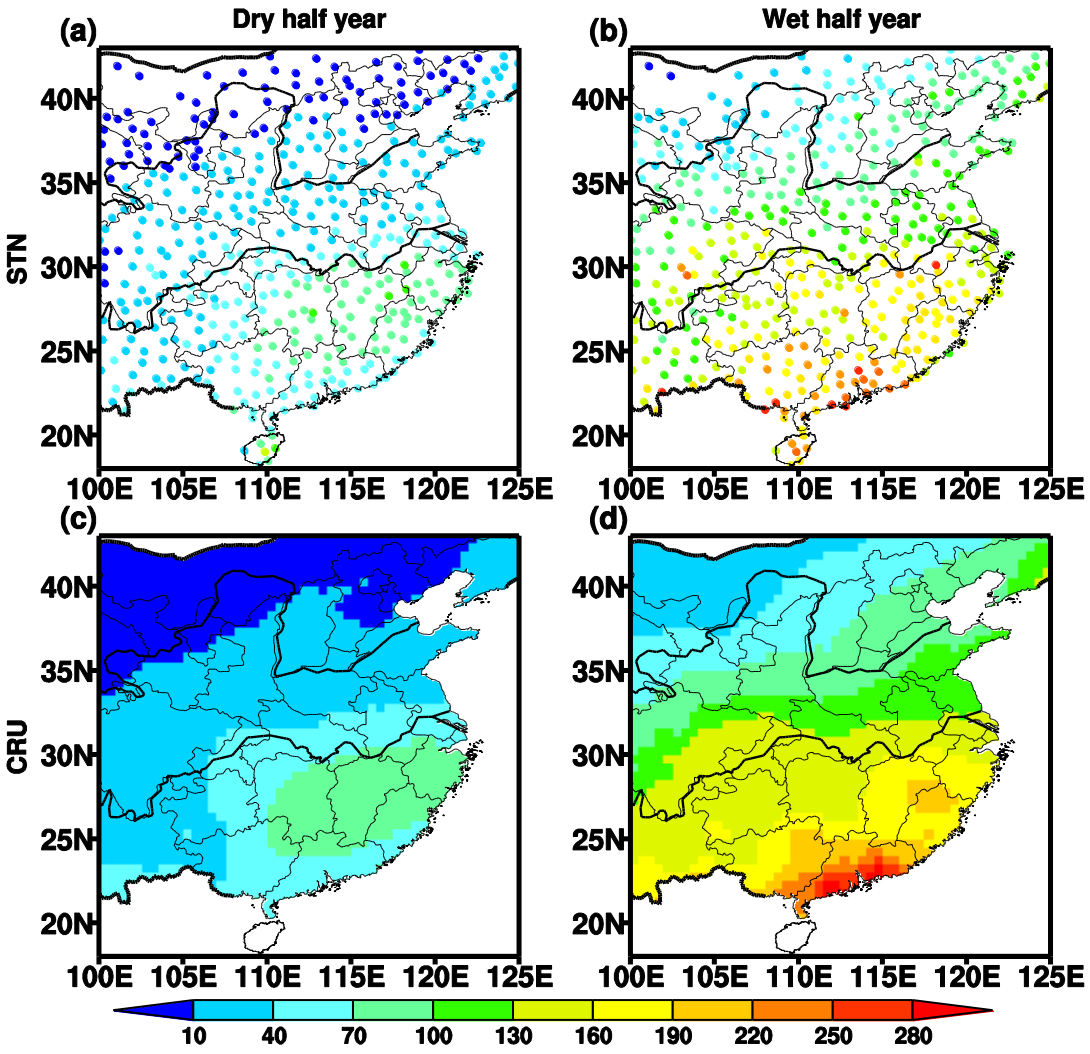

807

808 Figure 2. Spatial distribution of seasonal mean precipitation (mm/month) during

809 1960-2015 over eastern China from observation and CRU datasets, (a) and (c) are for

810 dry season; (b) and (d) are for wet season.

811

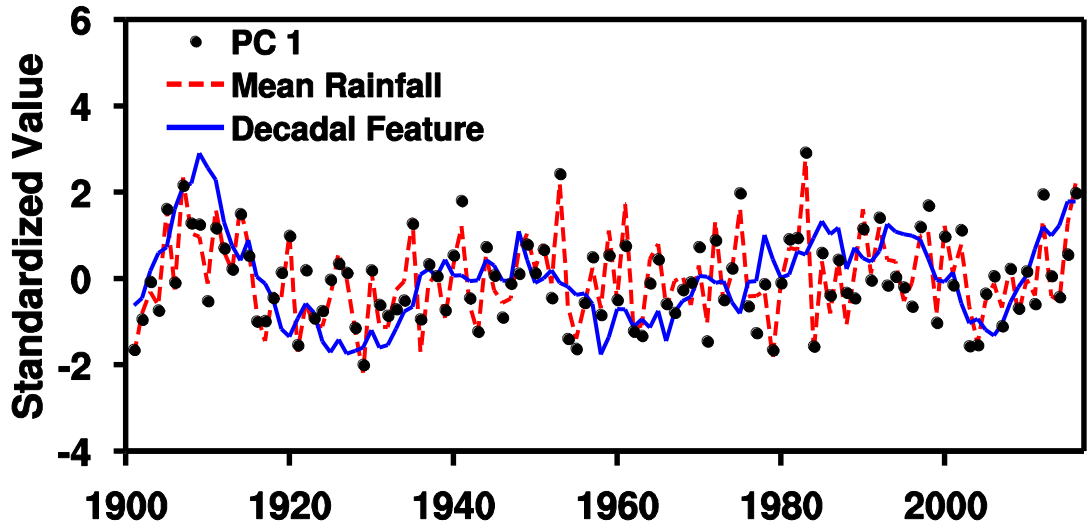

Figure 3. Standardized time series of all dry season precipitation over eastern China as shown in red dashed line, the black dots denote flipped PC1 and the blue lines denote the decadal features of dry season precipitation.

819

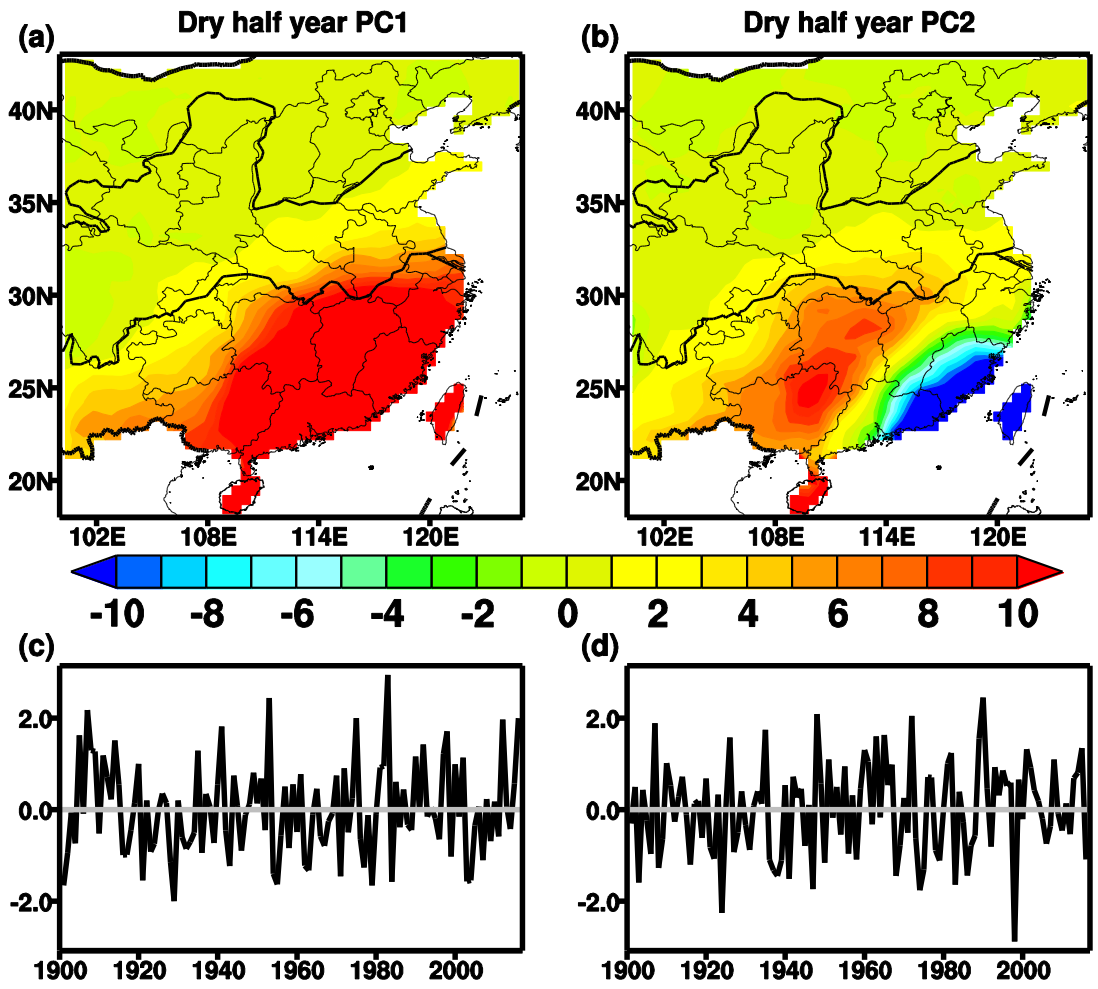

820

821 Figure 4. (a) The first and (b) second EOFs for the rainfall in dry season. (c) The first
822 and (d) second principal components (PCs) correspond to these EOFs from the
823 rainfall in dry season. Both time series are normalized with respect to the
824 corresponding standard deviations.

825

826

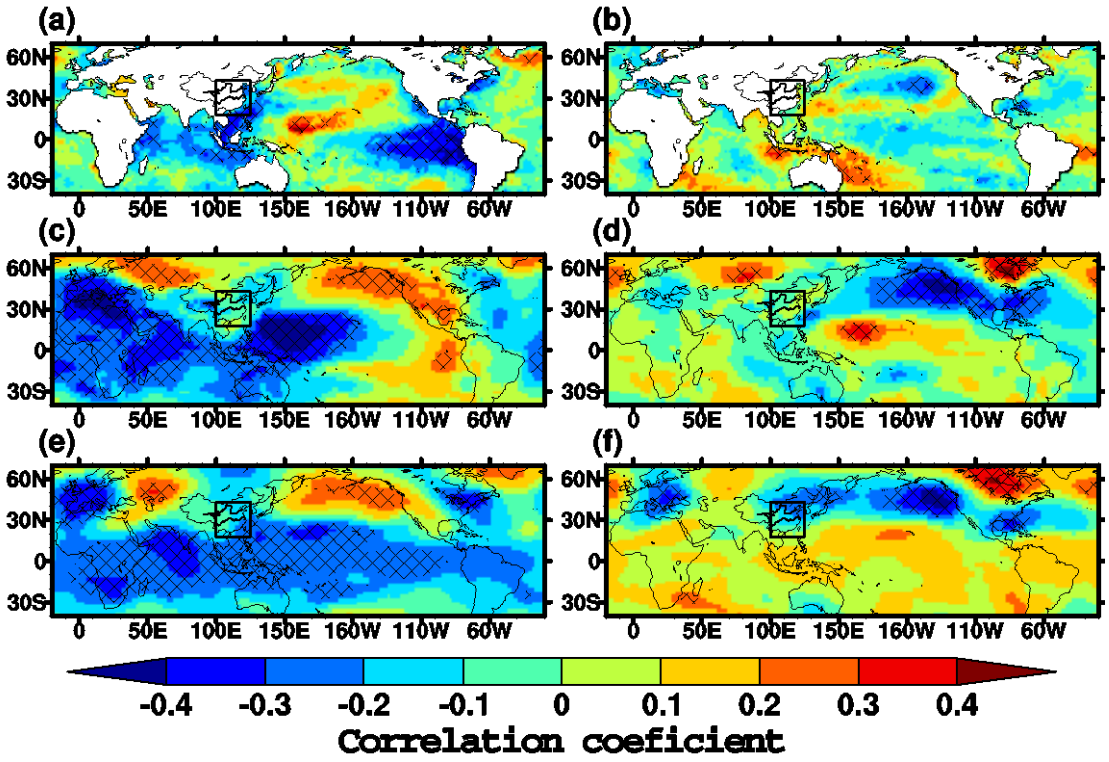

827

828 Figure 5. Correlation coefficients in dry season. (a) sea surface temperature and PC1,
829 (b) mean sea level pressure with PC1, (c) geopotential height at the 500 hPa and PC1,
830 (c) sea surface temperature and PC2, (e) mean sea level pressure with PC2 and (f)
831 geopotential height at the 500 hPa with PC2. Hatching denotes the regions with
832 statistical significance at the 95% confidence level. Black rectangle denotes the
833 eastern China.

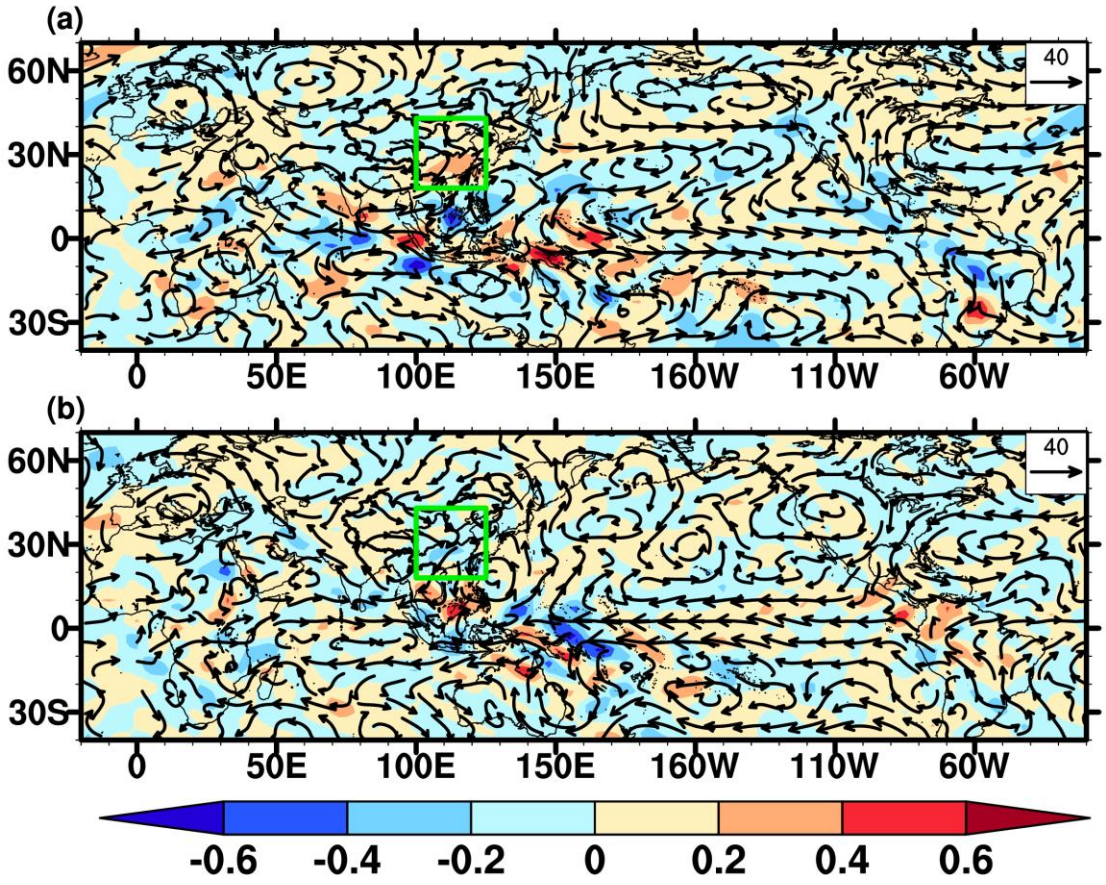

834

835 Figure 6. Vertically integrated water vapor anomalies (vector) and water vapor flux
836 divergence (shading) composited from the lightest 25th (a) and highest 75th (b)
837 percentile rainfall events in dry season. The water vapor flux unit is kg m^{-1} s^{-1} for and
838 the water vapor flux divergence is kg m^{-2} s^{-1}. Green rectangle denotes the eastern
839 China.

840

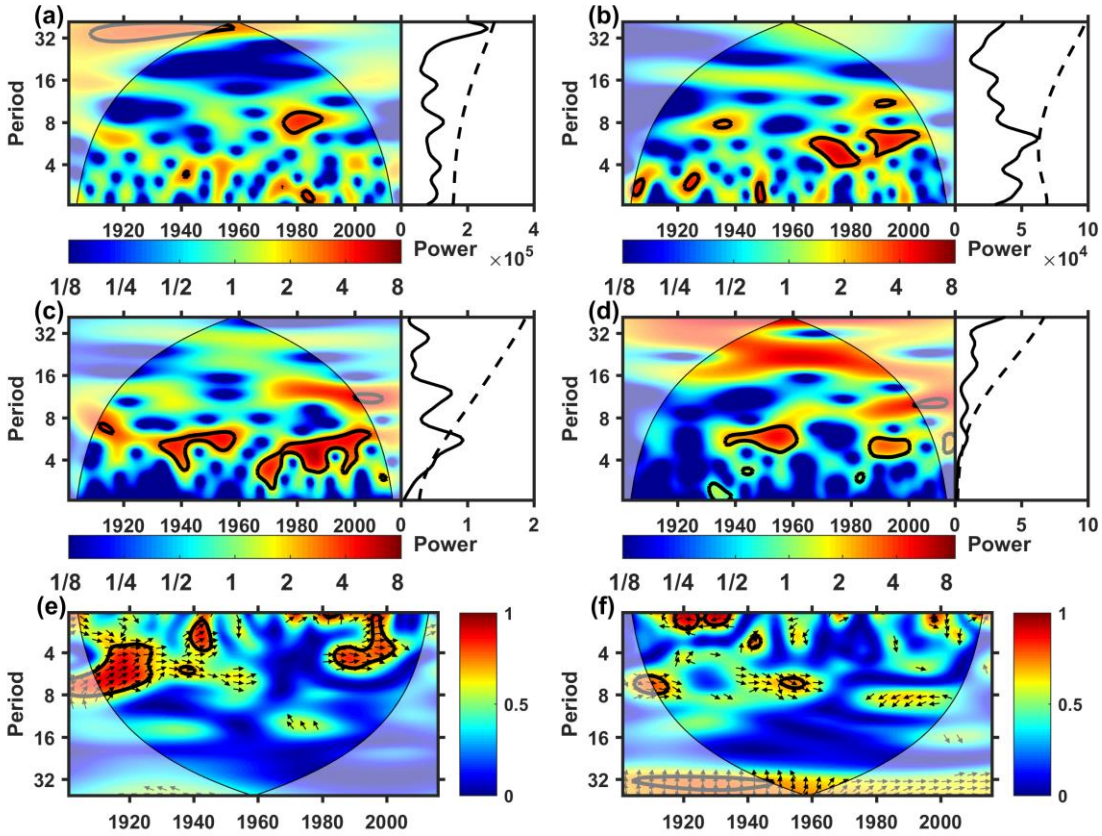

Figure 7. Wavelet spectra for dry season. (a) PC1, (b) PC2, (c) Niño3.4 index, (d) PDO index, (e) wavelet spectral coherence of PC1 and Niño3.4, and (f) wavelet spectral coherence of PC2 and PDO. The global spectra are shown on the right side of the time varying wavelet spectra and, the black lines denote the statistical significance at the 95% confidence level.

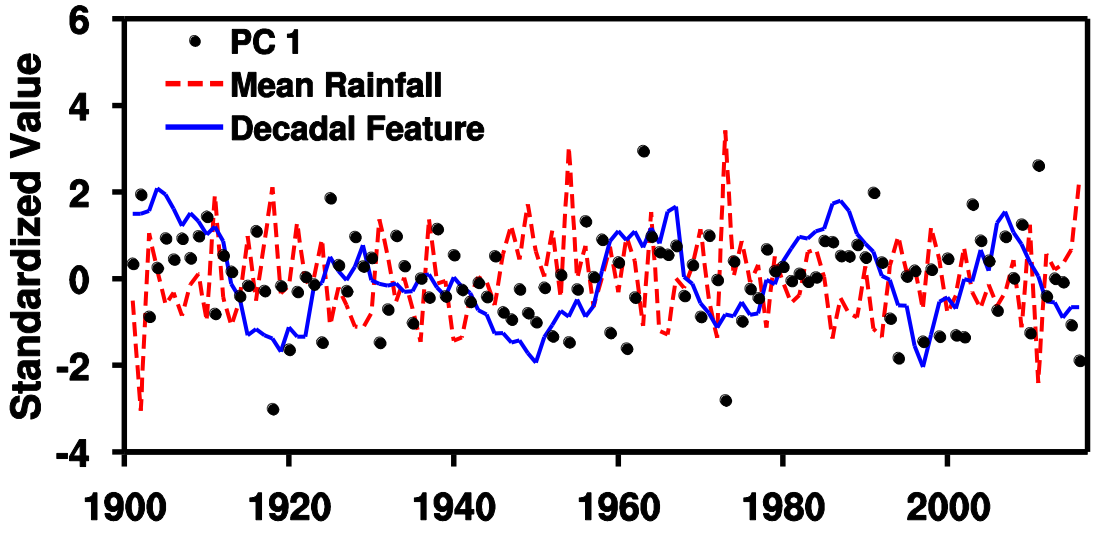

Figure 8. Standardized time series of all wet season precipitation over eastern China as shown in red dashed line, the black dots denote flipped PC1 and the blue lines denote the decadal features of wet season precipitation.

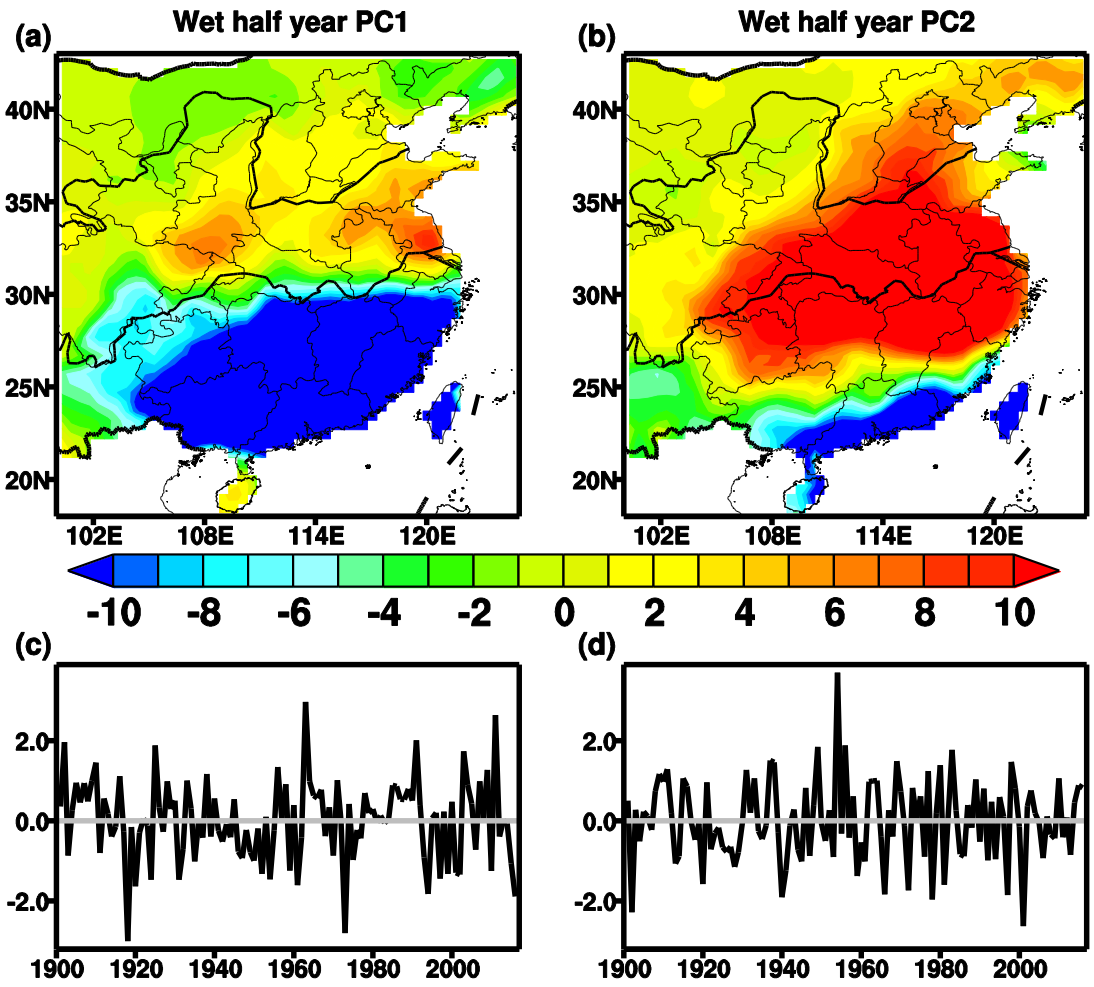

Figure 9. (a) The first and (b) second EOFs for the rainfall in wet season. (c) The first and (d) second principal components (PCs) correspond to these EOFs from the rainfall in wet season. Both time series are normalized with respect to the corresponding standard deviations.

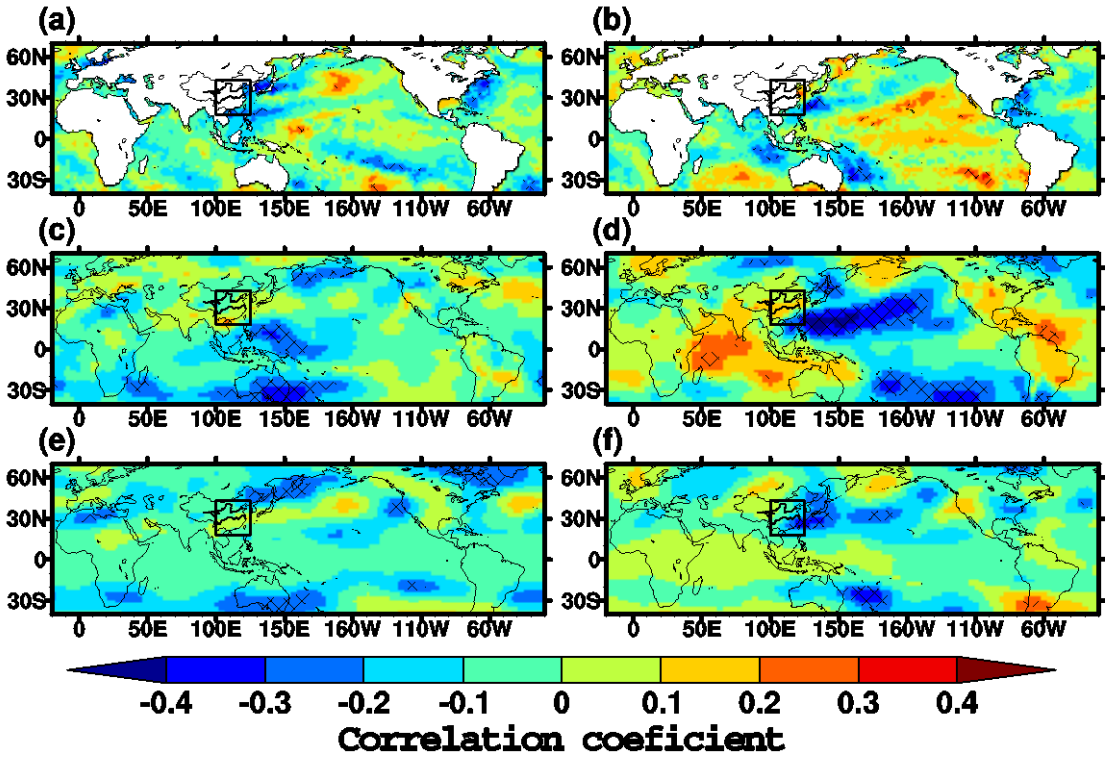

Figure 10. Correlation coefficients in wet season. (a) sea surface temperature and PC1, (b) mean sea level pressure with PC1, (c) geopotential height at the 500 hPa and PC1, (c) sea surface temperature and PC2, (e) mean sea level pressure with PC2 and (f) geopotential height at the 500 hPa with PC2. Hatching denotes the regions with statistical significance at the 95% confidence level. Black rectangle denotes the eastern China.

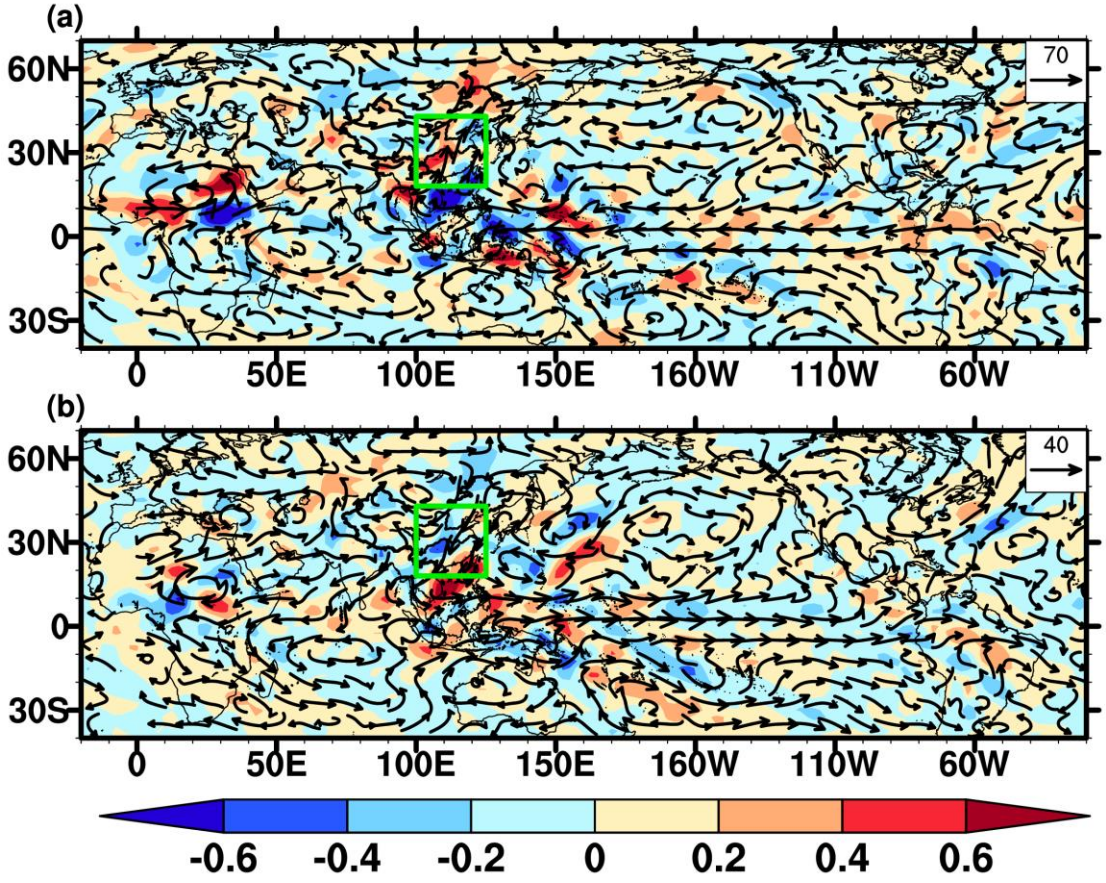

Figure 11. Vertically integrated water vapor anomalies (vector) and water vapor flux divergence (shading) composited from the lightest 25th (a) and highest 75th (b) percentile rainfall events in wet season. The water vapor flux unit is kg m^{-1} s^{-1} for and the water vapor flux divergence is kg m^{-2} s^{-1}. Green rectangle denotes the eastern China.

885

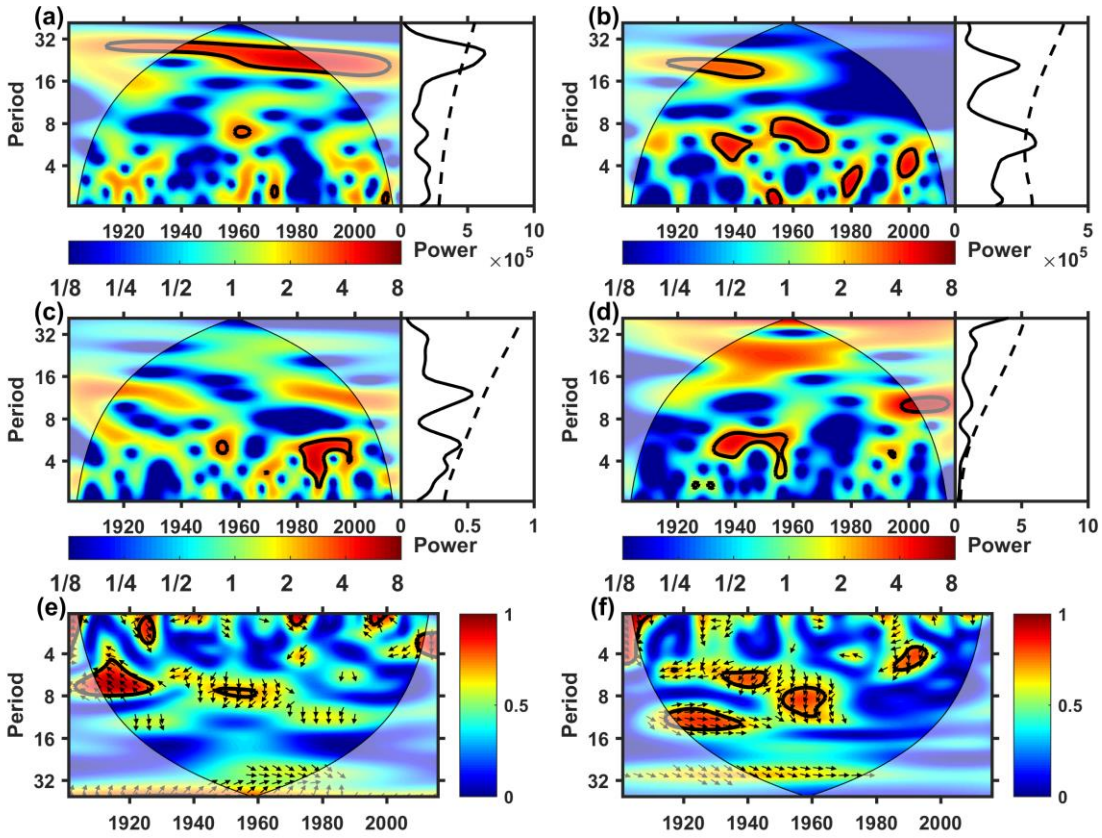

886

887 Figure 12. Wavelet spectra for wet season. (a) PC1, (b) PC2, (c) Niño3.4 index, (d)

888 PDO index, (e) wavelet spectral coherence of PC1 and Niño3.4, and (f) wavelet

889 spectral coherence of PC2 and PDO. The global spectra are shown on the right side of

890 the time varying wavelet spectra and, the black lines denote the statistical significance

891 at the 95% confidence level.

892

893

894

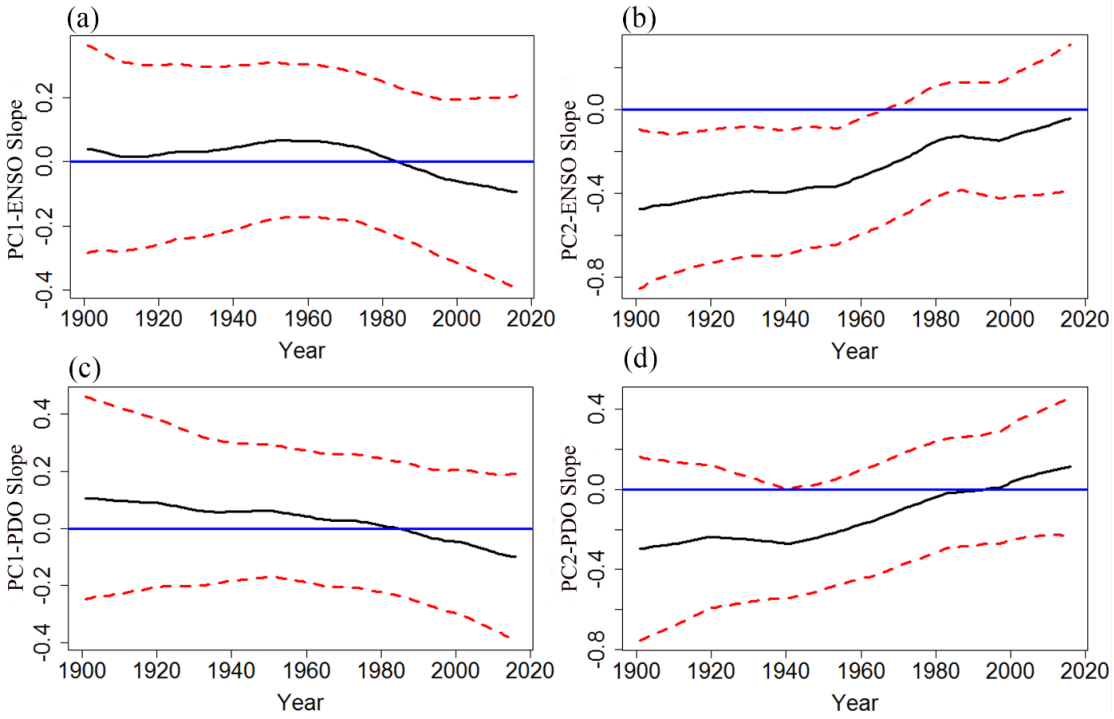

Figure 13. Changes in the relationships between rainfall and ENSO/PDO over time during 1901-2015. Black solid lines denote the estimated time-varying slopes, along with 25th and 75th percentile credible interval lines (red dashed lines) from the Bayesian dynamic linear model analysis.